FRB 20210405I: the first Fast Radio Burst sub-arcsecond localised with MeerKAT

Laura Nicole Driessen, Ewan Barr, David Buckley, Manisha Caleb, Hao Chen, Weiwei Chen, Mariusz Gromadzki, Fabian Jankowski, Renee Kraan-Korteweg, Michael Kramer, et al.

Monthly Notices of the ROYAL ASTRONOMICAL SOCIETY

MNRAS **527,** 3659–3673 (2024) https://doi.org/10.1093/mnras/stad3329
Advance Access publication 2023 November 2

FRB 20210405I: a nearby Fast Radio Burst localized to sub-arcsecond precision with MeerKAT

L. N. Driessen [1,2,3★] E. D. Barr,[4] D. A. H. Buckley [5,6,7] M. Caleb [3,8] H. Chen [6,9] W. Chen,[4] M. Gromadzki [10] F. Jankowski [2,11] R. C. Kraan-Korteweg,[6] J. Palmerio,[12] K. M. Rajwade [13] E. Tremou [14] M. Kramer,[2,15] B. W. Stappers [2] S. D. Vergani,[12] P. A. Woudt [6] M. C. Bezuidenhout [2,15] M. Malenta,[2] V. Morello [2,16] S. Sanidas,[2] M. P. Surnis[17] and R. P. Fender[18,6]

[1]*CSIRO, Space and Astronomy, PO Box 1130, Bentley, WA 6102, Australia*
[2]*Department of Physics and Astronomy, Jodrell Bank Centre for Astrophysics, The University of Manchester, Manchester, M13 9PL, UK*
[3]*Sydney Institute for Astronomy, School of Physics, The University of Sydney, NSW 2006, Australia*
[4]*Max-Planck-Institut für Radioastronomie, Auf dem Hügel 79, D-53121 Bonn, Germany*
[5]*South African Astronomical Observatory, PO Box 9, Observatory Rd, Observatory 7935, South Africa*
[6]*Department of Astronomy, University of Cape Town, Private Bag X3, Rondebosch 7701, South Africa*
[7]*Department of Physics, University of the Free State, PO Box 339, Bloemfontein 9300, South Africa*
[8]*ASTRO3D: ARC Centre of Excellence for All-sky Astrophysics in 3D, ACT 2601, Australia*
[9]*Research Center for Intelligent Computing Platforms, Zhejiang Laboratory, Hangzhou 311100, China*
[10]*Astronomical Observatory, University of Warsaw, Al. Ujazdowskie 4, PL-00-478 Warszawa, Poland*
[11]*LPC2E, Université d'Orléans, CNRS, 3A Avenue de la Recherche Scientifique, F-45071 Orléans, France*
[12]*GEPI, Observatoire de Paris, Université PSL, CNRS, 5 PlaceJules Janssen, F-92190 Meudon, France*
[13]*ASTRON, the Netherlands Institute for Radio Astronomy, Oude Hoogeveensedijk 4, NL-7991 PD Dwingeloo, the Netherlands*
[14]*National Radio Astronomy Observatory, Socorro, NM 87801, USA*
[15]*Centre for Space Research, North-West University, Potchefstroom 2531, South Africa*
[16]*SKA Observatory, Jodrell Bank, Lower Withington, Macclesfield, Cheshire, SK11 9FT, UK*
[17]*Department of Physics, Indian Institute of Science Education and Research Bhopal, Bhopal Bypass Road, Bhauri Bhopal 462066, Madhya Pradesh, India*
[18]*Department of Physics, Astrophysics, University of Oxford, Denys Wilkinson Building, Keble Road, Oxford OX1 3RH, UK*

Accepted 2023 October 27. Received 2023 October 11; in original form 2022 October 26

ABSTRACT

We present the first sub-arcsecond localized Fast Radio Burst (FRB) detected using MeerKAT. FRB 20210405I was detected in the incoherent beam using the MeerTRAP pipeline on 2021 April 05 with a signal to noise ratio of 140.8 and a dispersion measure of 565.17 pc cm^{-3}. It was detected while MeerTRAP was observing commensally with the ThunderKAT large survey project, and was sufficiently bright that we could use the ThunderKAT 8 s images to localize the FRB. Two different models of the dispersion measure in the Milky Way and halo suggest that the source is either right at the edge of the Galaxy, or outside. This highlights the uncertainty in the Milky Way dispersion measure models, particularly in the Galactic Plane, and the uncertainty of Milky Way halo models. Further investigation and modelling of these uncertainties will be facilitated by future detections and localizations of nearby FRBs. We use the combined localization, dispersion measure, scattering, specific luminosity, and chance coincidence probability information to find that the origin is most likely extra-galactic and identify the likely host galaxy of the FRB: 2MASS J1701249−4932475. Using SALT spectroscopy and archival observations of the field, we find that the host is a disc/spiral galaxy at a redshift of $z = 0.066$.

Key words: fast radio bursts – radio continuum: galaxies – radio continuum: transients.

1 INTRODUCTION

Fast radio bursts (FRBs) are short, bright, and coherent radio transients with durations on the order of milliseconds (see e.g. Cordes & Chatterjee 2019; Petroff, Hessels & Lorimer 2019; Caleb & Keane 2021; Chatterjee 2021; Petroff, Hessels & Lorimer 2022, for recent reviews). Most FRBs are observed as one-off events, though some are observed to repeat. Due to their transient nature and short-duration, localizing one-off events to less than a few arcseconds remains a challenge.

The first FRB to be localized, FRB 20121102A, was a repeater. This repeating nature allowed it to ultimately be localized to 0.″1 (Chatterjee et al. 2017; Marcote et al. 2017) and associated it with a faint, continuum radio source which exhibits flux variability of tens of percent on day time-scales. Tendulkar et al. (2017) imaged the position of the FRB with the Gemini North telescope, revealing a dwarf galaxy at a redshift of $z = 0.19273(8)$. This galaxy has a low metallicity and shows no signs of active galactic nucleus

★ E-mail: laura.driessen@sydney.edu.au

(AGN) activity. Very long baseline interferometry (VLBI) follow-up observations with milliarcsecond resolution revealed a projected linear separation of $\lesssim 40$ pc between the source of the FRBs and the persistent continuum radio source with the latter having a projected size of $\lesssim 0.7$ pc (Marcote et al. 2017). All together, the observations suggest that the source of the FRBs could be associated with a low-luminosity AGN or a young neutron star powering a supernova remnant (Chatterjee et al. 2017; Marcote et al. 2017). The case of FRB 20121102A demonstrates how important localization is for identifying host galaxies and unveiling local environments, ultimately shedding light on the physical processes leading to the burst production.

With the advent of intereferometeric searches, FRBs are now almost routinely being localized upon discovery without having to rely on repeaters for precise localization. There were ∼800 published FRBs in the Supernova Working Group Transient Name Server[1] (TNS) at the time of writing, of which 57 are known repeaters. Presently, 27 FRBs have been conclusively localized to a host galaxy. Nineteen of these FRBs (Bannister et al. 2019; Prochaska et al. 2019; Bhandari et al. 2020; Heintz et al. 2020; Macquart et al. 2020; Bhandari et al. 2022; James et al. 2022b; Bhandari et al. 2023; Gordon et al. 2023; Ryder et al. 2023) were detected and localized using the Australian Square Kilometre Array Pathfinder (ASKAP; Hotan et al. 2021), four (Chatterjee et al. 2017; Law et al. 2020; Luo et al. 2020; Niu et al. 2022) have been localized using the Karl G. Jansky Very Large Array (VLA; Perley et al. 2011), two (Bhardwaj et al. 2021; Marcote et al. 2021; Kirsten et al. 2022; Nimmo et al. 2022b) have been localized using Very Long Baseline Interferometry (VLBI) both using the European VLBI network (EVN; Marcote et al. 2020), one has been localized using the Deep Synoptic Array 10-dish (DSA-10) prototype (Ravi et al. 2019), and one (Ravi 2023) has been localized with the DSA-110 prototype. Seven of the 27 localized FRBs are repeaters. Upon investigating the global properties of a sample of FRB host galaxies, Bhandari et al. (2022) and Gordon et al. (2023) found no significant difference between the host galaxies of repeating and non-repeating FRBs.

Localization reveals important information about FRBs and their hosts, and gives us clues about their progenitors and immediate environments. Some progenitor models for FRB 20121102A include a young neutron star in a compact supernova remnant or a neutron star near the accretion torus of a black hole (Chatterjee et al. 2017; Michilli et al. 2018; Zhang 2018). The localization of the repeating FRB 20200120E (Kirsten et al. 2022) to a globular cluster in the M81 galactic system requires an unusual magnetar progenitor model for FRBs as globular clusters consist of older stars, not the young population expected for magnetars. If we can determine the position of an FRB progenitor, we can also determine if the FRB passed through the halo of an intervening galaxy. Prochaska et al. (2019) used one such event FRB to constrain the halo gas density, magnetization and turbulence of the intervening galaxy. Macquart et al. (2020) demonstrated that a large sample of arcsecond-localized FRBs can be used to directly measure the baryons in the universe.

MeerKAT (Camilo et al. 2018) is an interferometer in the Karoo region of South Africa. It consists of 64 × 13.5 m dishes and has baselines up to 8 km, resulting in a field of view (FoV) of ∼1 square degree and resolution of better than ∼ 5″ at 1400 MHz. MeerKAT currently has two receivers installed, the L-band receiver (856–1712 MHz) and the UHF receiver (580–1015 MHz) and can observe in modes with 1024, 4096, or 32 000 channels.

The Meer(more) TRAnsients and Pulsars (MeerTRAP; Sanidas et al. 2018; Bezuidenhout et al. 2022; Jankowski et al. 2022; Rajwade et al. 2022) project at the MeerKAT telescope undertakes fully commensal, high-time resolution radio transient searches simultaneously with all of the ongoing MeerKAT Large Survey Projects (LSPs).

ThunderKAT (Fender et al. 2016) is the MeerKAT LSP searching for, and investigating, radio transient and variable sources in the image-plane. ThunderKAT observes and monitors known variable radio sources such as X-ray binary systems (e.g. Russell et al. 2019; Bright et al. 2020; Williams et al. 2020; van den Eijnden et al. 2022), follows up sources that were initially detected at other wavelengths (Hewitt et al. 2020; Rhodes et al. 2020; Driessen et al. 2022b), and performs untargeted searches for transient and variable sources in the FoV of MeerKAT image-plane observations (Driessen et al. 2020; Andersson et al. 2022; Rowlinson et al. 2022; Driessen et al. 2022a).

In this paper, we present the detection and localization of FRB 20210405I the first sub-arcsecond localization of an FRB using MeerKAT. In Section 2, we describe the MeerTRAP and ThunderKAT radio observations. In Section 3, we present the detection and properties of FRB 20210405I. In Sections 5 and 6 we summarize and conclude.

2 RADIO OBSERVATIONS

2.1 MeerTRAP pipeline

For the observations presented in this paper, MeerKAT was observing at an L-band centre frequency of 1284 MHz with a usable bandwidth of ∼770 MHz. Single pulses are searched for simultaneously in incoherent and coherent modes using the MeerTRAP backend. In the coherent mode, the voltages from the inner 40–44 dishes of the ∼1-km core of the array are coherently combined to 764 coherent beams (CBs) on sky with a total FoV of ∼0.4 deg^2. A CB typically has a FWHM of ∼ 43″ but can vary in size depending on the elevation of the telescope at the time of observation. In the incoherent mode the intensities of all the available 64 MeerKAT dishes are summed to create a less sensitive incoherent beam (IB) but with a much wider FoV of ∼1.3 deg^2. The CBs typically tile the IB with beams touching where the sensitivity is 25 per cent of the peak CB sensitivity.

The output data stream of the F-engine are captured, delay corrected, phased, and channelized before being sent over the network to the Filterbanking Beam-former User Supplied Equipment (FBFUSE) that was designed and developed at the Max Planck Institute for Radio Astronomy in Bonn. Typically, for L-band observations FBFUSE combines the data into 764 total-intensity tied-array beams. The data are then captured at 306.24 μs time resolution by the Transient User Supplied Equipment (TUSE), a real-time transient detection backend instrument developed by the MeerTRAP team at the University of Manchester. The GPU-based single pulse search pipeline AstroAccelerate[2] (Armour et al. 2012; Adámek & Armour 2020) is used to search for bursts in real-time after incoherently dedispersing the data in the DM range 0–5118.4 pc cm^{-3} (see Caleb et al. 2020, for more details).

2.2 ThunderKAT imaging

The ThunderKAT observations presented here are targeted observations of the low-mass X-ray binary GX 339−4. ThunderKAT has been observing this source on a weekly cadence since September

[1] https://www.wis-tns.org/

[2] https://github.com/AstroAccelerateOrg/astro-accelerate

2018 and continued to do so until August 2023 (Tremou et al. 2020). The high cadence and length of the monitoring campaign make this an excellent field for performing commensal searches for variable and transient sources (Driessen et al. 2020, 2022a).

The ThunderKAT GX 339−4 observations are taken using the MeerKAT L-band receivers in full-polarisation mode. The shortest integration time available for most imaging observations is 8 s. The L-band receivers have a bandwidth of 856 MHz with a central frequency of 1284 MHz. The bandpass and flux calibrator, PKS J1934−638, is observed for 5 min at the start of the observing block and the phase calibrator, PMN J1726−5529, is observed for 2 min before and after the target scan. The target is typically observed for 10 min.

The imaging data were processed using standard methods including flagging with `AOFlagger`[3] (Offringa 2010; Offringa, van de Gronde & Roerdink 2012) and calibration, including phase correction, antenna delays, and band-pass corrections, using the Common Astronomy Software Application[4] (CASA; McMullin et al. 2007). Further details on the processing methods can be found in Driessen et al. (2020) and Tremou et al. (2020).

In order to image as well as possible over short time intervals, we produced an image mask using a deep, combined MeerKAT image of the GX 339−4 field made by jointly imaging the visibilities with `DDFacet` (Tasse et al. 2018) from 8 epochs (a commissioning observation from April 2018 and the weekly epochs from September and October 2018) for a total integration time of 3.63 h. The data were then imaged with `WSClean` (Offringa et al. 2014) utilizing the image mask. Images of the single epoch, full integration time as well as the shortest integration time (8 s), were made. We included multiscale cleaning, a Briggs robust weight of −0.7 (Briggs 1995) and three w-projection plane layers. To maximize the signal-to-noise ratio (S/N) we performed a multifrequency synthesis (MFS) clean using 8 frequency channels and a 4$^{\text{th}}$ order spectral polynomial fit. We also produced subband images by removing the spectral fit and MFS imaging parameters, resulting in 8 subband images with central frequencies: 909, 1016, 1123, 1230, 1337, 1444, 1551, 1658 MHz. We then primary beam corrected the sub-band images by dividing them by primary beam models.

Searching for variables and transients in ThunderKAT images was performed using the the `LOFAR Transients Pipeline` (`TraP`, Release 4.0; Swinbank et al. 2015). The `TraP` is software designed with LOFAR[5] specifically in mind. It extracts light curves for radio sources from a time series of fits images. We used the default `TraP` parameters[6] with some small adjustments. We forced the `TraP` to search for sources consistent with the Gaussian synthesized beam shape and required that sources be separated by three beamwidths to be considered unique. In other work searching for variable sources in this field (see Driessen et al. 2022a) we manually identified resolved sources and artefacts. We removed these sources in our analysis.[7]

We searched for interesting sources in the `TraP` light curves using three variability parameters: η_ν, V_ν, and $\xi_{\nu,\max}$. The η_ν parameter is based on the reduced χ^2 statistic, where the model light curve assumes that the flux density is constant:

$$\eta_\nu = \frac{1}{N-1}\sum_{i=1}^{N}\frac{\left(I_{\nu,i}-\overline{I_\nu}\right)^2}{\sigma_{\nu,i}^2} = \frac{N}{N-1}\left(\overline{wI^2}-\frac{\overline{wI}^2}{\overline{w}}\right), \quad (1)$$

where N is the number of measurements, $I_{\nu,i}$ is the flux density for epoch i, $\overline{I_\nu}$ is the mean flux density, and w is the weight ($w = 1/\sigma_{\nu,i}^{2\ 2}$ where $\sigma_{\nu,i}^2$ are the 1σ uncertainties). We therefore expect a constant source to have a η_ν close to one. The V_ν parameter is the standard deviation of the light curve divided by the mean of the light curve and as such measures the spread of the flux density measurements. The $\xi_{\nu,\max}$ parameter is based on the median and the median absolute deviation (MAD) of the light curve where the MAD is given by

$$\text{MAD} = \text{median}\left(\left|I_{\nu,i}-\widetilde{I_\nu}\right|\right), \quad (2)$$

where $\widetilde{I_\nu}$ is the median flux density. The ξ value is then calculated using

$$\xi_i = \frac{I_{\nu,i}-\widetilde{I_\nu}}{\text{median}\left(\left|I_{\nu,i}-\widetilde{I_\nu}\right|\right)} \quad (3)$$

and the $\xi_{\nu,\max}$ value is the resulting maximum value of the set ξ_i. A high $\xi_{\nu,\max}$ indicates a short, bright outburst and is useful for detecting transients.

2.2.1 *Absolute astrometry*

We corrected the absolute astrometry of the radio sources in the GX 339−4 field using the method described in Driessen et al. (2022a). We used the PYTHON Blob Detector and Source Finder[8] (`pyBDSF`) to determine the positions of sources in an image, which we used to determine and correct the accuracy of our absolute astrometry. We used Australian Telescope Compact Array (ATCA) Parkes-MIT-NRAO (PMN) sources (ATPMN; McConnell et al. 2012) within the MeerKAT FoV to correct the astrometry. The ATPMN survey has a median absolute astrometric uncertainty of 0.″4 in both Right Ascension (RA) and Declination (Dec.) when compared to the Long Baseline Array (LBA) Calibrator Survey (LCS1; Petrov et al. 2011) and the International Celestial Reference Frame (ICRF; Ma et al. 1998). Both LCS1 and ICRF use the International Celestial Reference System (ICRS).

To determine our astrometric accuracy, we solved for a transformation matrix, A to shift and rotate the MeerKAT sources to match the positions of the ATPMN sources.[9] If X represents the uncorrected coordinates and $X^{'}$ represents the corrected coordinates, then we are solving for A:

$$X^{'} = XA \quad (4)$$

$$\begin{bmatrix} RA_1^{'} & DEC_1^{'} & 1 \\ RA_2^{'} & DEC_2^{'} & 1 \\ RA_N^{'} & DEC_N^{'} & 1 \end{bmatrix} = \begin{bmatrix} RA_1 & DEC_1 & 1 \\ RA_2 & DEC_2 & 1 \\ RA_N & DEC_N & 1 \end{bmatrix} \begin{bmatrix} a_1 & a_2 & 1 \\ b_1 & b_2 & 1 \\ c_1 & c_2 & 1 \end{bmatrix}, \quad (5)$$

where A is an affine transformation matrix that includes scale, shear, and translation.

[3] https://sourceforge.net/projects/aoflagger/
[4] https://casa.nrao.edu/
[5] The transients key project: https://transientskp.org/
[6] The default settings for the pipeline configuration and job configuration files can be found in the TraP documentation.
[7] See https://github.com/AstroLaura/MeerKAT_LightCurve_Analysis for the code for extracting the source information from `TraP`.
[8] https://www.astron.nl/citt/pybdsf/
[9] The code for performing the astrometric corrections can be found on GitHub: https://github.com/AstroLaura/MeerKAT_Source_Matching

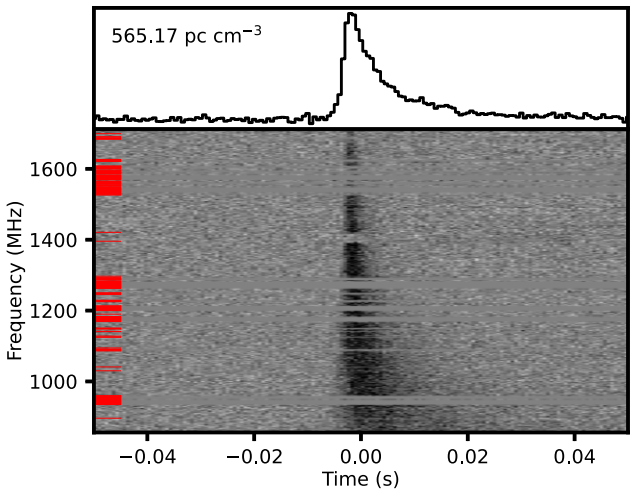

Figure 1. Dynamic spectrum of FRB 20210405I. The lower panel shows the time and frequency. The top panel shows the frequency averaged burst profile. The profile has been de-dispersed to the scattering-corrected DM of 565.17 pc cm^{-3}. The S/N-maximizing DM is 566.43 pc cm^{-3}. The red lines indicate frequency channels that have been masked due to RFI. The dropout of the FRB signal around 1.4 GHz that can be seen in both the dynamic and the total intensity spectrum in Fig. 4 is instrumental in nature. The time samples in that ∼30 MHz frequency range are delayed by about 1.25 s with respect to the rest of the data. This is a known issue that used to happen in exceptional cases when one or more beamformer nodes dropped out of sync with the rest of the cluster, thereby delaying their signal. The frequency width of the shifted signal of 2 × 856 MHz/64 = 26.75 MHz indicates that two logical nodes (one physical server) were affected.

We then applied A to the coordinates of all sources in the field. In the case of the 8 s integration images, we determined the astrometric correction for the full integration (usually 10 min) image and applied that correction to the 8 s slices.

3 FRB 20210405I

FRB 20210405I was detected while MeerTRAP was observing commensally with ThunderKAT during an observation of GX 339−4 on 2021 April 05 at 04:14:40 UTC. The pulse, shown in Fig. 1, was extremely bright, and was detected by the MeerTRAP real-time transient pipeline in the IB as well as several hundred CBs, implying a nearby origin. The pulse was brightest in the IB, and we obtain an optimized S/N of 140.8 corresponding to a S/N-maximizing DM of 566.43 pc cm^{-3} using the MTCUTILS[10] package or a scattering-corrected DM of 565.17 pc cm^{-3}. The scattering-corrected DM is the DM which gives the minimum pulse width when scattering, intrinsic width and dispersion measure smearing has been accounted for. The expected Galactic DM contribution is ∼350 pc cm^{-3} using the YMW16 Galactic free-electron model (Yao, Manchester & Wang 2017) or ∼500 pc cm^{-3} using the NE2001 Galactic free-electron model (Cordes & Lazio 2002). We assume a conservative halo DM contribution of 144 ± 60 pc cm^{-3} (with a 40 per cent uncertainty) as the source is close to the Galactic plane (Yamasaki & Totani 2020). Here we will present the properties of FRB 20210405I, with a summary shown in Table 1.

[10]https://bitbucket.org/vmorello/mtcutils/

Table 1. Properties of FRB 20210405I.

FRB Parameter	Unit measured	
MJD_{topo} [a]		59309.1768572970
UTC_{topo} [a]		2021 Apr 05 04:14:40.470
Beam		IB
RA	(hms)	$17^h01^m21^s.5 \pm 0''.4$
Dec.	(dms)	$-49°32'42''.8 \pm 0''.5$
l	(deg)	338.1920
b	(deg)	−4.5969
S/N-maximizing DM	(pc cm^{-3})	566.43
Scattering-corrected DM	(pc cm^{-3})	565.17
S/N		140.8
W_{50p} [a]	(ms)	9.79 ± 0.23
W_{10p} [a]	(ms)	23.80 ± 0.53
τ_s^a	(ms)	8.67 ± 0.28
W_{eq}^a	(ms)	11.81 ± 0.23
Project physical offset	(kpc)	10.65
	Instrumental	
t_{dm} [b]	(ms)	6.3
N_{chan}		1024
$N_{ant,\,ib}$		60
LSP		ThunderKAT
	Inferred	
S_{peak}	(Jy)	15.9
F	(Jy ms)	120.8
$DM_{mw,\,ne2001}$	(pc cm^{-3})	516.1
$DM_{mw,\,ymw16}$	(pc cm^{-3})	348.7
DM_{halo}	(pc cm^{-3})	144
$DM_{xg,\,ne2001}$	(pc cm^{-3})	50.3
$DM_{xg,\,ymw16}$	(pc cm^{-3})	217.7
z		0.066

Notes.[a] Measured at 1016.5 MHz.
[b] Intrachannel dispersive smearing in the lowest frequency channel.

3.1 Localization

The high detection S/N of FRB 20210405I meant that we could utilize the ThunderKAT imaging observations to localize it. The imaging observation had an observation time of 10 min, with a minimum integration time of 8 s. The pulse has a dispersion delay of ∼1.4 s, which is fully contained within one 8 s image. As described in subsection 2.2, we made a full time integration MFS image and 74 × 8 s image slices using `WSClean`.

We applied the `TraP` to the 8 s images. The resulting variability parameters are shown in Fig. 2. We can see that the known mode-changing pulsar, PSR J1703−4851 (Wang, Manchester & Johnston 2007; Jankowski et al. 2019), is an outlier in all three parameters (see Driessen et al. 2022a, for the light curve of PSR J1703−4851). There is also another outlier in these plots that is more extreme in the V_ν and $\xi_{\nu,\,max}$ parameters compared to PSR J1703−4851, and has a lower median flux density. This outlier was detected in a single 8 s image, centred in time on 2021 April 05, T: 04:14:42.2, which matches the time that MeerTRAP detected FRB 20210405I. An image of the burst is shown in Fig. 3 (left panel). As it was the only outlier in the variability parameters apart from known source PSR J1703−4851, was detected in a single epoch, and was detected at the time of FRB 20210405I, we identified this source as FRB 20210405I.

We corrected the astrometry using the method described in subsection 2.2.1. We determined the transformation matrix, A, using

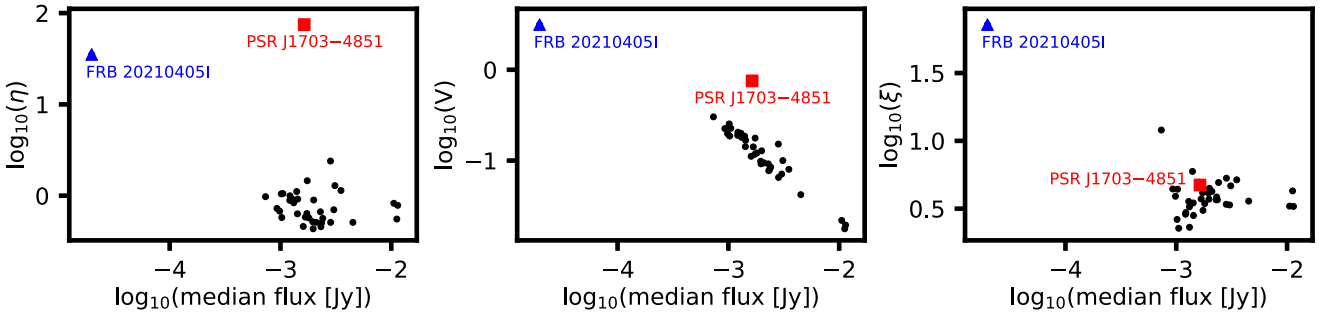

Figure 2. Variability parameters (described in subsection 2.2) for all sources in the 8 s images from 2021 April 05. PSR J1703−4851 (labelled) is an outlier. The other, lower flux density outlier is FRB 20210405I.

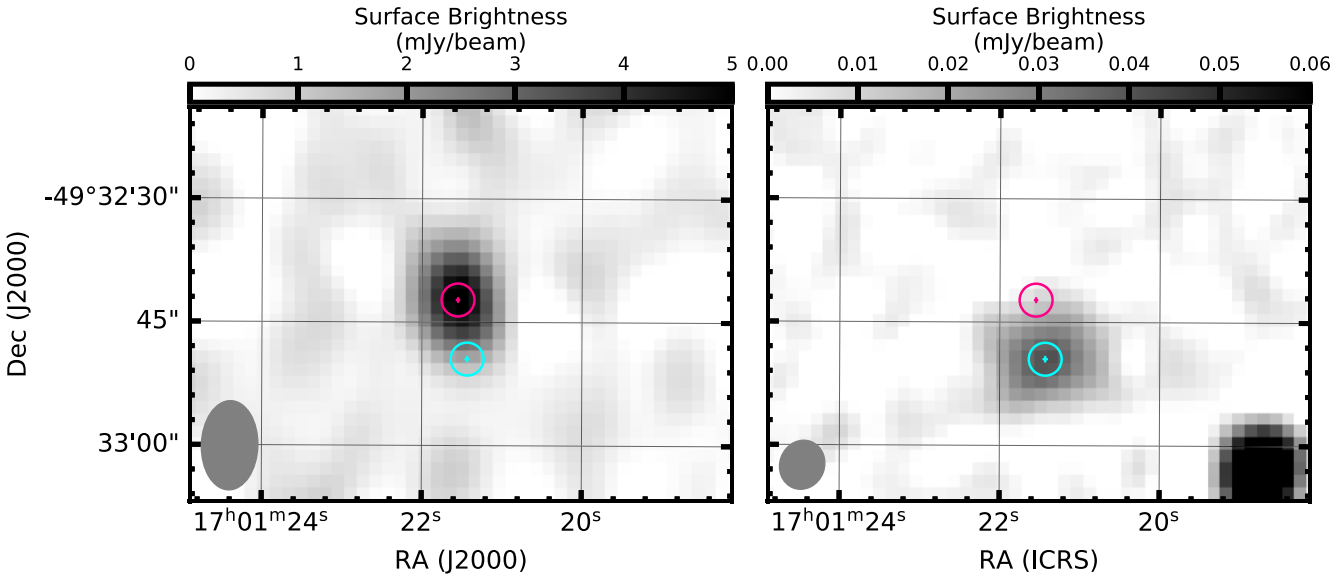

Figure 3. MeerKAT images of the position of FRB 20210405I. The left panel shows the 8 s MeerKAT MFS image where FRB 20210405I was detected and localized. The position of FRB 20210405I is marked with the magenta circle (2″radius) and cross hairs. The right panel shows the 3.63 h combined image of the GX 339−4 field, with the location of the continuum source MKT J170121.4−493250 marked with cyan circle (2″radius) and cross hairs. For both sets of cross hairs the size of the cross hairs reflects the sizes of the uncertainties on the positions. The synthesized beam is shown in the bottom left of each panel.

Table 2. Separation between the ATPMN and MeerKAT reference sources before and after applying the transformation. The MeerKAT positions were extracted from the full, 10 min integration image. The separation is given in arcseconds.

ATPMN source name	Separation before (″)	Separation after (″)
J165418.2−481303	0.6	0.4
J165613.1−492318	0.6	0.2
J165614.9−472915	0.2	0.2
J165908.3−481548	0.1	0.1
J171154.9−491250	0.4	0.07

the 10 min image:

$$A = \begin{bmatrix} 1.0 & -3.8 \times 10^{-3} & 1.0 \\ 8.5 \times 10^{-5} & 1.0 & 1.0 \\ -1.2 \times 10^{-2} & 2.1 \times 10^{-3} & 1.0 \end{bmatrix}. \quad (6)$$

The separations between the MeerKAT sources and ATPMN sources before and after correcting the astrometry are shown in Table 2. We then applied the transformation matrix to the 8 s image containing FRB 20210405I. To confirm that the correction to the 10 min image was applicable to the 8 s images we compared the positions of the bright sources in the field between the full integration time and 8 s images. We found that the median offset of the positions was 0.″2, which is less than the 0.″4 uncertainty on the ATPMN positions. As such the uncertainty on the astrometry is the 0.″4 arcsecond absolute astrometric uncertainty from the ATPMN positions. After applying the correction, the position of FRB 20210405I was determined to be RA: $17^{h}01m21^{s}.5$ (255.33970°) and Dec.: −49°32′42.″5 (−49.54515°). The uncertainty on the RA and Dec. found by `pyBDSF` was 0.″1 and 0.″2, respectively; however, the uncertainty on the astrometric correction was 0.″4 in both RA and Dec. We added these uncertainties in quadrature to find that the uncertainty on the position of FRB 20210405I is 0.″4 in RA and 0.″5 in Dec. The burst is 47′30″ from GX 339−4 and 47′ 48″ from the phase centre of the observation.

3.2 Flux density and fluence

FRB 20210405I was detected 47′ 48″ from the phase centre of the observation. This means that we need to take the attenuation of the IB into account. We use the modified single-pulse radiometer

equation (Dewey et al. 1985) from Jankowski et al. (2023) to do this

$$S_{\rm peak}\left({\rm S/N}, {\rm W_{eq}}, \vec{a}\right) = {\rm S/N}\,\beta\,\eta_{\rm b}\,\frac{T_{\rm sys}+T_{\rm sky}}{G\sqrt{b_{\rm eff}N_{\rm p}{\rm W_{eq}}}}\,a_{\rm CB}^{-1}\,a_{\rm IB}^{-1}, \quad (7)$$

where $S_{\rm peak}$ is the peak flux density, S/N = 140.8 is the signal-to-noise, $\beta = 1$ is the digitization factor, $\eta_{\rm b} = 1$ is the beam-forming efficiency, $T_{\rm sys} = 19$ K and $T_{\rm sky} = 7.8$ K are the system and sky temperatures respectively, $G = 0.335$ is the gain of the IB, $b_{\rm eff} = 670.4$ MHz is the effective frequency bandwidth, $N_{\rm p} = 2$ is the sum of the number of polarisations, ${\rm W_{eq}} = 7.6 \times 10^{-3}$ s is the observed equivalent width of the boxcar pulse, and $a_{\rm CB}^{-1}$=1 and $a_{\rm IB}^{-1} = 1/0.22$ are the CB and IB attenuation factors respectively that take into account the angular dependence of the beam response. $a_{\rm CB}^{-1}$=1 as we only consider the IB detection in detail here. Using these values results in $S_{\rm peak} = 15.9$ Jy and a fluence of $F = 120.8$ Jy ms. These values are shown in Table 1.

3.3 Scattering

We analysed the highest-S/N total intensity pulse profile of FRB 20210405I recorded by the MeerTRAP backend by fitting a scattering model to the frequency sub-banded data. The model consisted of a normalized Gaussian profile convolved with a single-sided exponential pulse broadening function that is characteristic for scattering in the thin-screen regime of turbulent ionized media (e.g. Cordes & Lazio 2001). We performed the profile fits using a custom PYTHON-based software called SCATFIT[11] (Jankowski 2022). It utilizes the Levenberg–Marquardt minimization algorithm as implemented in LMFIT (Newville et al. 2016) for an initial fit, after which it explores the posterior using the EMCEE Markov chain Monte Carlo sampler (Foreman-Mackey et al. 2013). For more details about the fitting technique, see Jankowski et al. (2023). As the pulse broadening is significant, we first estimated the scattering-corrected DM from the data split into eight frequency sub-bands, which is 565.17 ± 0.49 pc cm^{-3}. To determine the uncertainty we combined in quadrature the half width at which the S/N versus trial DM curve decreased by unity with the error in ΔDM derived from the scattering fit. The best-fitting scattering index is -4.6 ± 0.1, which we can see as the solid line in Fig. 4.

3.4 Continuum radio emission

We searched the 3.63 h joint image (see subsection 2.2) for continuum radio emission near the position of FRB 20210405I. The joint image was astrometrically corrected using the method described in subsection 2.2 using the same sources shown in Table 2. The transformation matrix for the joint image is

$$A = \begin{bmatrix} 1.0 & 4.4\times10^{-5} & 1.0 \\ -1.1\times10^{-4} & 1.0 & 1.0 \\ -2.9\times10^{-3} & -1.2\times10^{-2} & 1.0 \end{bmatrix}. \quad (8)$$

A faint, slightly resolved continuum source, MKT J170121.4−493250, is identified 7.″4 from the position of FRB 20210405I, shown in Fig. 3 (right panel). The uncorrected coordinates of the resolved source are RA: $17^{\rm h}01^{\rm m}21\overset{\rm s}{.}4$s (255.33932°) and Dec.: −49°32′50.″0 (−49.54708°). The astrometrically corrected coordinates of MKT J170121.4−493250 are RA: $17^{\rm h}01^{\rm m}21\overset{\rm s}{.}4$s (255.33926°) and Dec.: −49°32′50.″2 (−49.54727°) with combined PYBDSF and astrometric uncertainty of 0.″6 in RA and 0.″5 in Dec. The offset between the uncorrected and corrected position is 0.″7. MKT J170121.4−493250 is too faint to be detected in sub-band images, unlike FRB 20210405I, where we can apply a primary beam correction. It is only detected in the joint MFS image. The uncorrected PYBDSF total flux density of this source is $150 \pm 4\,\mu$Jy.

4 OPTICAL OBSERVATIONS

A Dark Energy Camera Plane Survey (DECaPS; Schlafly et al. 2018) VR stacked optical image is shown in Fig. 5 with the same magenta (FRB 20210405I) and cyan (MKT J170121.4−493250) cross hairs as shown in Fig. 3. The VR filter is a broad-band filter from 497 to 756 nm. Stacked images are combined images from multiple exposures. Optical sources from *Gaia* Data Release 3 (*Gaia* DR3; *Gaia* Collaboration et al. 2016, 2023) that have *Gaia* DR3 distances have also been labelled in Fig. 5. Schlafly et al. (2018) found that the typical difference between DECaPs source positions and *Gaia* source positions is 0.″1 and *Gaia* is tied to the ICRS. Despite FRB 20210405I being located in the Zone of Avoidance (ZoA), we can see a faint extended optical source coincident with the position of MKT J170121.4−493250. This suggests that the extended, continuum radio emission is associated with this extended optical source. The ZoA is the part of the sky that is strongly affected by Galactic foreground extinction. In the ZoA the foreground extinction causes background galaxies to appear smaller as isophotal diameters are strongly affected (see e.g. Riad, Kraan-Korteweg & Woudt 2010). We can also see in Fig. 5 that FRB 20210405I is 0.″3 from a bright optical source, *Gaia* DR3 5938235492995353728, that has a *Gaia* DR3 distance of $780.6^{+80.2}_{-98.5}$ pc (*Gaia* Collaboration et al. 2023).

Optical spectroscopy of the extended optical source and *Gaia* DR3 5938235492995353728 was undertaken with the Southern African Large Telescope (SALT; Buckley, Swart & Meiring 2006) using the Robert Stobie Spectrograph (RSS; Burgh et al. 2003). Data reductions were done using PYSALT version 0.47, the PYRAF-based software package for SALT data reductions (Crawford et al. 2010),[12] which includes gain and amplifier cross-talk corrections, bias subtraction, amplifier mosaicking, and cosmetic corrections. Spectral reductions (object extraction, wavelength calibration, and background subtraction) were all done using standard IRAF[13] routines, including relative flux calibration.

Two repeat 1150 s exposures were taken of *Gaia* DR3 5938235492995353728 on 2021 April 15 in clear conditions with seeing of 1.″8. The low-resolution PG300 grating was used, covering the region 3800–8400 Å, with a slit width of 1.″25, resulting in a spectral resolution of 17 Å. The combined spectrum appears to be a G or K type star, with an obvious Mg b line at 5172 Å and no presence of molecular bands, ruling out a later spectral type.

A SALT spectroscopic observation of the extended optical source coincident with MKT J170121.4−493250 was obtained on 2021 September 02 in clear conditions with 1.″3 seeing using the same PG300 grating, but with a 2″ slit, giving a resolution of 24 Å. The position of the slit, chosen to reduce contamination from *Gaia* DR3 5938235492995353728, is shown in Fig. 5. Two repeat 1600 s exposures were taken. This object is a galaxy, with prominent Hα and [S II] emission lines at $z = 0.066$ (see Fig. 6). The Hα value suggests that it is consistent with a star-forming spiral galaxy. The

[11] Version 0.2.14, https://github.com/fjankowsk/scatfit/

[12] https://astronomers.salt.ac.za/software/pysalt-documentation/

[13] https://iraf.noao.edu/

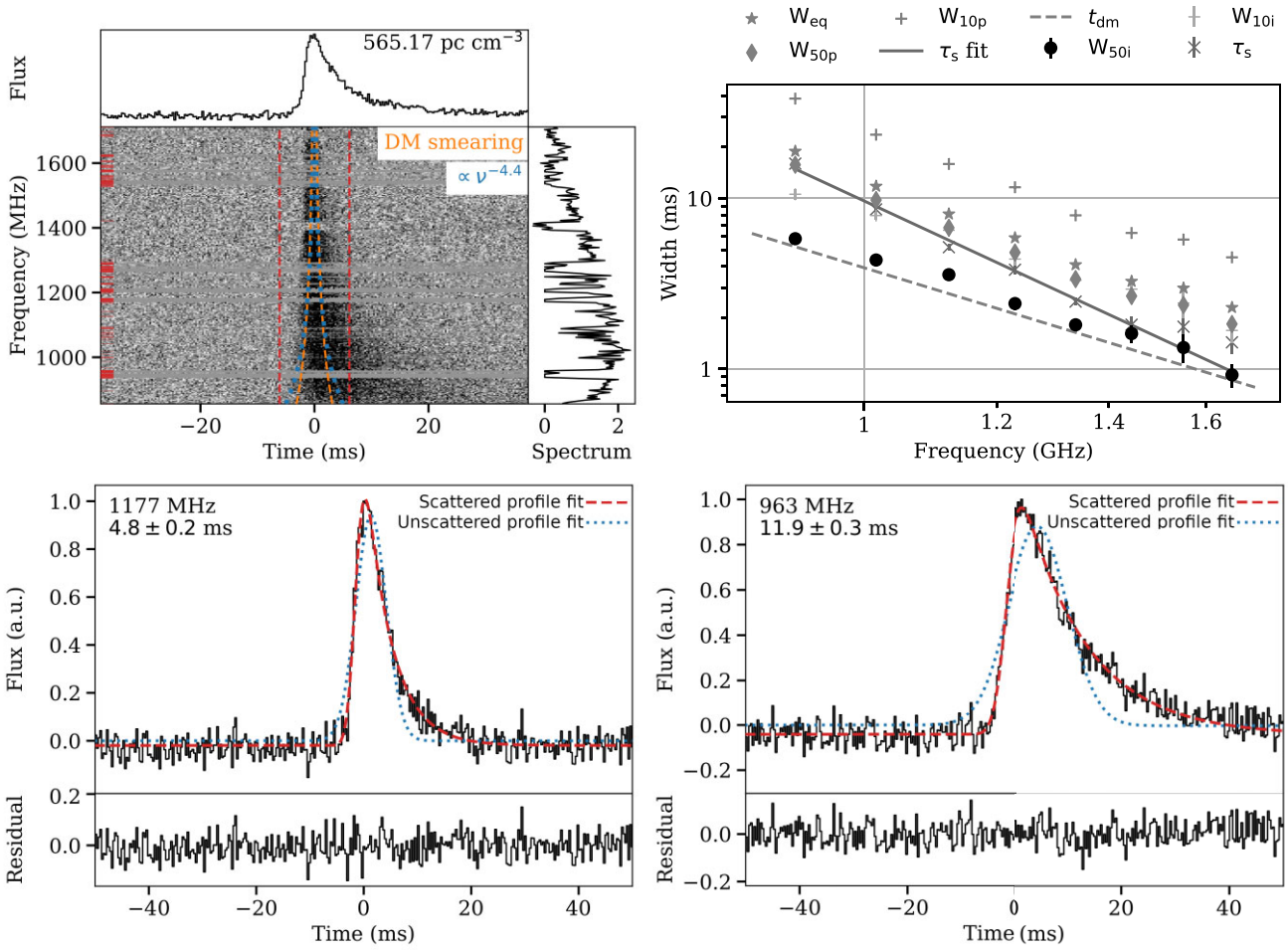

Figure 4. Scattering analysis of FRB 20210405I. The MeerTRAP filterbank data were dedispersed at the scattering-corrected DM of 565.17 pc cm^{-3}. Top left: Dedispersed dynamic spectrum, pulse profile, and uncalibrated total intensity spectrum. The data are displayed at their native time resolution, but we summed every four frequency channels for clarity. The horizontal red lines indicate the masked channels, and the vertical-dashed lines indicate the on-pulse region used to compute the spectrum. We used an orange-dashed line to mark the pulse broadening due to instrumental DM smearing. We used a blue-dashed line to mark the pulse-broadening $\propto \nu^{-4.4}$, where ν is the observing frequency, representative of scattering in Kolmogorov-turbulent ionized media. Top right: The post-scattering pulse widths W_{50p} and W_{10p}, the Gaussian intrinsic widths W_{50i} and W_{10i}, the boxcar equivalent widths W_{eq}, and the scattering times τ_s as a function of frequency. We show the expected DM smearing times (dashed line) and the best-fitting power law to the τ_s data (solid line). Bottom left: Pu°se profile in a sub-band of 214 MHz centred at 1177 MHz with the best scattered profile fit (red-dashed line) and the best unscattered Gaussian fit (blue-dotted line) overlaid. The residuals are computed with respect to the scattering model and appear white. Bottom right: The same at 963 MHz.

disc of the galaxy is likely obscured by extinction ($A_V = 2.41$ at the position of FRB 20210405I; Schlafly & Finkbeiner 2011).

We also examined the point spread function (PSF) of *Gaia* DR3 5938235492995353728, shown in Fig. 7(b), and compared it to the PSFs of other sources in the field, shown in panels (d)–(f) of Fig. 7. The PSFs of all of these sources show no evidence of excess emission in the wings and can be described as Gaussians.

4.1 Properties of the extended optical source

The optical galaxy is faint in the optical, visible as an extended blob in the stacked VR image shown in Fig. 5. It is coincident with the continuum extended radio source MKT J170121.4−493250. It is also in the ZoA with high extinction and partially obscured by a bright foreground star. It is only because of the sensitivity of DECam that we could detect the galaxy at all in the optical. While the obscuring star and faintness make optical analysis challenging, we can investigate the source in other bands. An extended source is visible in the 2 Micron All Sky Survey (2MASS; Skrutskie et al. 2006), particularly in the K band. The J and H bands are likely dominated by contamination from the nearby star. It is identified as a galaxy, 2MASS J1701249−4932475, and has an extinction corrected ($A_K = 0.265$) apparent magnitude of ∼14.4. Using the SALT distance, this corresponds to an absolute K-band magnitude of ∼−22.8, which is also consistent with a spiral galaxy. The galaxy is visible as an extended source in the WISE W1 band, with WISE colours W1 − W2 ∼ −0.169 and W2 − W3 ∼ 3.67. This places it between where normal disc galaxies and star-forming galaxies are located in the WISE color-color diagram (Fig. 12 in Wright et al. 2010). This agrees with the SALT Hα detection.

Using the SALT spectrum, we determined the Hα line flux by simultaneously fitting Hα and the surrounding N II doublet with three Gaussian profiles to the continuum-subtracted spectrum, excluding regions of sky absorption. We obtained $F_{H\alpha} = (1.9 \pm 0.1) \times 10^{-16}$ erg s^{-1} cm^{-2}, which corresponds to a star formation rate limit (SFR) $\gtrsim 0.02$ M$_\odot$ yr^{-1} at $z = 0.066$ (SFR $\gtrsim 0.1$ M$_\odot$ yr^{-1} correcting

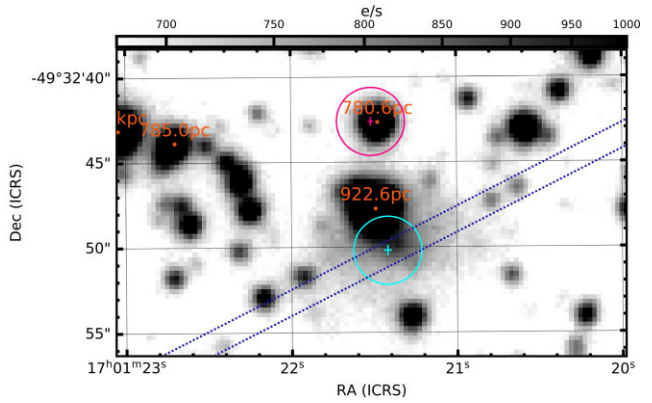

Figure 5. DECaPS VR stacked optical image showing the astrometrically corrected positions of the FRB 20210405I burst (magenta circle and cross hairs as in Fig. 3) and continuum radio source MKT J170121.4−493250 (cyan circle and cross hairs as in Fig. 3). Optical sources detected by the *Gaia* DR3 mission with distance values, where available, are labelled in orange. The blue-dotted lines show the RSS slit position.

for the Galactic extinction), considering a Salpeter (1955) initial mass function (IMF). These values should also be corrected for the dust extinction of the FRB host galaxy. We estimated this by measuring the flux limit of the Hβ flux and comparing it to the Hα over Hβ Balmer ratio. We found significant dust extinction with $A_V > 1.8$. We corrected the Hα flux for dust extinction in the host galaxy using a Milky Way extinction curve by Pei (1992) and obtained $F_{H\alpha} > (3.4 \pm 0.1) \times 10^{-15}$ erg s^{-1} cm^{-2}, corresponding to an SFR $\gtrsim 0.3$ M$_\odot$ yr^{-1}. Using the absolute K band magnitude ~ -22.8 and the mass–luminosity relation of galaxies, we estimated a stellar mass of $\log(M_*/M_\odot) = 11.25$. Using this value and the dust corrected SFR determined above, we obtained a specific star formation rate limit (sSFR, defined as SFR/M$_*$) of $\log(\mathrm{sSFR}) > -11.7$ yr^{-1}. Finally, using the flux of the N II λ6584, we estimated the metallicity $12 + \log(\mathrm{O/H}) = 9.0^{+0.2}_{-0.1}$, using the strong line ratio with Hα and following Maiolino et al. (2008).

We used a two-hour MeerKAT observation of the GX 339−4 field from 2021 April 07 to search for H I emission from MKT J170121.4−493250. Using the redshift of the extended optical source, $z = 0.066$, we find that the expected H I frequency is 1.3324 GHz; however, we do not detect any H I emission. This is likely because the galaxy lies nearly a degree from the phase centre of the MeerKAT observations, which is outside the primary beam and is therefore challenging to detect. The rms noise of the H I cube is 0.23 mJy beam^{-1} channel^{-1} prior to primary beam correction and 1.15 mJy beam^{-1} channel^{-1} after primary beam correction. The beam size in the H I cube is $16\farcs45 \times 7\farcs00 \sim 20.8 \times 8.9$ kpc. We derived the 3σ upper limit on the H I flux of the likely host galaxy using

$$S_{\mathrm{HI\_ul}} = 3 \times rms \times W \times \sqrt{\frac{W_0}{W}}\,, \tag{9}$$

where $S_{\mathrm{HI\_ul}}$ is in the units of Jy km s^{-1}, rms is in units of Jy beam^{-1} channel^{-1} for the H I cube after primary beam correction, W is the velocity width of the H I emission for the likely host galaxy in units of km s^{-1}, W_0 is 44.5 km s^{-1} (the channel width of the H I data cube). By assuming W is 400 km s^{-1} and the H I disc is smaller than the beam size (20.8×8.9 kpc), $S_{\mathrm{HI\_ul}}$ is 0.46 Jy km s^{-1}. The H I mass upper limit for the likely host galaxy is 8.4×10^9 M$_\odot$, given by Meyer et al. (2017):

$$M_{\mathrm{HI\_ul}} = \frac{2.35 \times 10^5}{(1+z)^2} \times D_L^2 \times S_{\mathrm{HI\_ul}}, \tag{10}$$

where $M_{\mathrm{HI\_ul}}$ is in M$_\odot$, $S_{\mathrm{H\,I}}$ is the H I flux upper limit in Jy km s^{-1}, z is the redshift (0.066) and D_L is the luminosity distance of the galaxy in Mpc (296.8 Mpc is used for $z = 0.066$ and assuming $H_0 = 70$ km s^{-1} Mpc^{-1}, $\Omega_M = 0.3$, $\Omega_{vac} = 0.7$).

5 DISCUSSION

5.1 Is FRB 20210405I Galactic or extra-galactic?

We have detected and localized FRB 20210405I using the MeerTRAP pipeline and ThunderKAT images. However, there is a discrepancy between the Milky Way DM contributions from the YMW16 model (348.7 pc cm^{-3}) and the NE2001 model (516.1 pc cm^{-3}), that may place FRB 20210405I (∼566 pc cm^{-3}) either just outside the galaxy, or inside the halo. Here we will present the properties of FRB 20210405I to determine if the source is Galactic or if it originates from the identified candidate galaxy: 2MASS J1701249−4932475.

5.1.1 Nearby star Gaia *DR3 5938235492995353728*

The *Gaia* DR3 distance of *Gaia* DR3 5938235492995353728 is 780^{+80}_{-100} pc. Using the YMW16 electron density model, a source in that direction within the Milky Way Galaxy at that distance would have a DM of ∼24 pc cm^{-3} compared to the DM of FRB 20210405I: ∼566 pc cm^{-3}. The PSF of *Gaia* DR3 5938235492995353728 is a Gaussian that matches the PSF of point sources in the field. This indicates that the source is a point source as expected for a star and that there is no evidence of a galaxy directly behind and obscured by *Gaia* DR3 5938235492995353728. Due to the spectral confirmation of *Gaia* DR3 5938235492995353728 as a star, the distance to it, and the lack of evidence of an extended source directly behind the star in the PSF, we conclude that the position match between FRB 20210405I and *Gaia* DR3 5938235492995353728 is a chance coincidence.

Gaia DR3 5938235492995353728 is 0.″3 from the position of FRB 20210405I. The star's coordinates, after accounting for proper motion, are RA: $17^h01m21\overset{s}{.}477 \pm 1$ mas and Dec.: $-49°32'42\farcs688 \pm 1$ mas. The median offset between *Gaia* counterparts of the third realization of the International Celestial Reference Frame (ICRF; Charlot et al. 2020) sources is 0.5 mas (*Gaia* Collaboration et al. 2022). While the uncertainty on the star's position is small, the uncertainty on FRB 20210405I's position is 0.″5 in RA and 0.″4 in Dec. (taking the astrometric uncertainty into account). *Gaia* DR3 5938235492995353728 is a G or K type star, so we can assume that it is a similar star to our Sun. Using the equations in Tiburzi et al. (2021), the radius at which the solar wind produces a DM of 60 pc cm^{-3}, accounting for the difference between the FRB 20210405I DM and the NE2001 MW DM, is 0.1 au. At a distance of 780^{+80}_{-100} pc this is a disc of radius $0.13^{+0.02}_{-0.01}$ mas. This is significantly smaller than the uncertainty on the star's position. Even if we assume that *Gaia* DR3 5938235492995353728 could produce significant DM contributions at 1 au the radius of the disc at 780^{+80}_{-100} pc would be $1.3^{+0.2}_{-0.1}$ mas. Given that the radius of the possible stellar wind is at least two orders of magnitude smaller than the uncertainty on the FRB position it is unlikely that FRB 20210405I passed close enough to the star for any possible stellar winds to have a significant impact on the DM of the FRB.

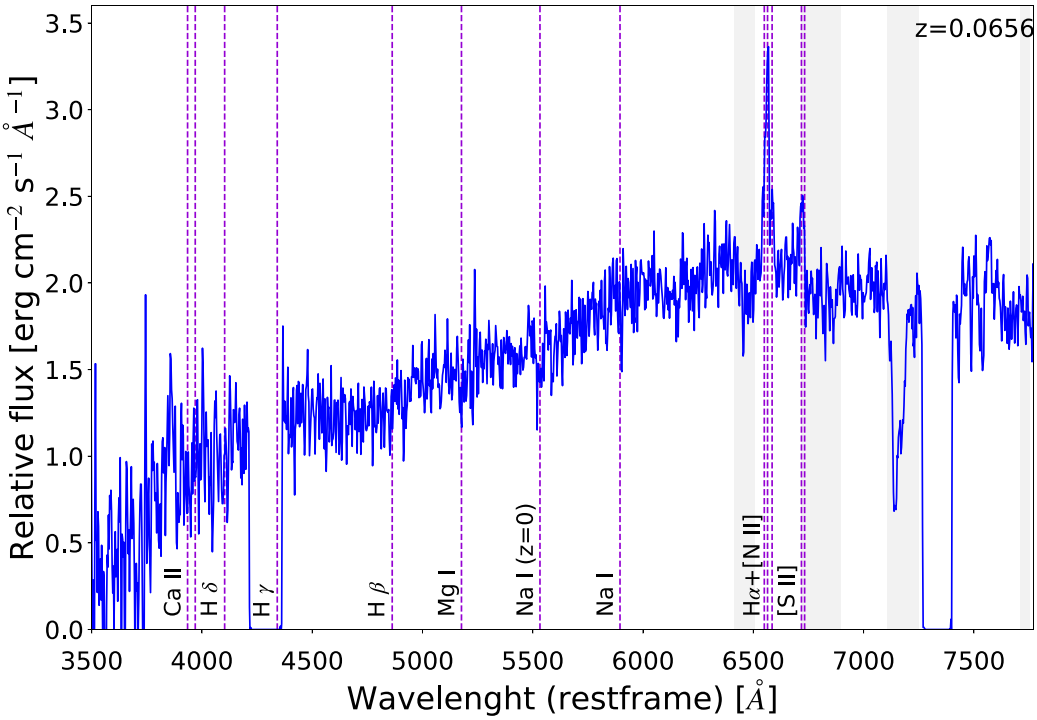

Figure 6. SALT spectrum of the extended optical source. Specific lines are indicated with dashed-purple lines, and telluric lines are highlighted in grey.

5.1.2 Dispersion measure

We can use the DM to explore whether the FRB progenitor is likely in the galaxy or in the Milky Way Halo. We use a halo DM of $144 \pm 60\,\mathrm{pc\,cm^{-3}}$ from Yamasaki & Totani (2020) including a 40 per cent uncertainty. This is because FRB 20210405I is at a Galactic latitude of $b = -4.597$ deg or $\sin|b| = 0.08$. Constraining the DM of the halo, particularly near the Galactic plane, is challenging. Recently, Cook et al. (2023) presented a comparison of halo DM models and reviewed them using FRB DMs. While they only presented models with $\sin|b| > 0.5$, they found that the Yamasaki & Totani (2020) halo model is consistent with their FRB observations.

The ISM contributions computed using the NE2001 and YMW16 Galactic free electron models differ significantly. If we assume a 20 per cent uncertainty on the maximum integrated ISM DM contribution and a 40 per cent uncertainty on the MW halo DM contribution (the halo is more poorly understood) for the FRB 20210405I sightline, the probabilities of FRB 20210405I being extra-galactic are ∼24 and ∼80 per cent for the NE2001 and the YMW16 model, respectively. We visualize this in Fig. 9.

We can use the DM inventory to consider whether the different DM contributions are feasible. The YMW16 DM excess is $\mathrm{DM_{FRB}} - \mathrm{DM_{MW,YMW16}} = 217\ \mathrm{pc\,cm^{-3}}$ and the NE2001 DM excess is $\mathrm{DM_{FRB}} - \mathrm{DM_{MW,NE2001}} = 50\ \mathrm{pc\,cm^{-3}}$. We assume that the uncertainty on these DMs is 20 per cent. The expected cosmic DM for $z = 0.06$ is $\mathrm{DM_{cosmic}} = 51^{+82}_{-25}\ \mathrm{pc\,cm^{-3}}$using the Macquart relation (James et al. 2022a). If we use the YMW16 DM and assume that FRB 20210405I is associated with the galaxy at $z = 0.066$ then $\mathrm{DM_{host}} = \mathrm{DM_{FRB}} - \mathrm{DM_{halo}} - \mathrm{DM_{ISM}} - \mathrm{DM_{cosmic}} = 565.17 - 144 \pm 58 - 349 \pm 70 - 51^{+82}_{-25} = 21^{+122}_{-94}\ \mathrm{pc\,cm^{-3}}$. Assuming the same values but using NE2001 for the $\mathrm{DM_{ISM}}$ gives $\mathrm{DM_{host}} = -145^{+144}_{-121}\ \mathrm{pc\,cm^{-3}}$. The uncertainties on these host DM values are large as the DMs along the line of sight are not well known. The 1σ upper limit on the NE2001 $\mathrm{DM_{ISM}}$ is $-1\ \mathrm{pc\,cm^{-3}}$; however, the range of possible $\mathrm{DM_{host}}$ values using YMW16 for $\mathrm{DM_{ISM}}$ is plausible.

However, we would require an impossible, negative $\mathrm{DM_{host}}$ if we use the NE2001 model for $\mathrm{DM_{ISM}}$.

We need to account for DM excesses of 217 ± 58 and $50 \pm 103\ \mathrm{pc\,cm^{-3}}$ for YMW16 and NE2001, respectively if we assume that FRB 20210405I is inside the Milky Way. An unidentified H II region could account for these DM excesses; therefore, it is not possible to conclusively rule out that FRB 20210405I originated from inside the galaxy based on the DM alone.

5.1.3 Scattering

Fig. 8 shows the scattering time, τ_s, measurement of FRB 20210405I interpolated to 1 GHz in a τ_s – DM diagram. We highlight the expected DM contribution from the Milky Way (MW), $\mathrm{DM_{MW}} = 516 \pm 103\ \mathrm{pc\,cm^{-3}}$, with its 20 per cent uncertainty range for that sightline as computed using the NE2001 Galactic free-electron model. Additionally, we show the combined range of $\mathrm{DM_{MW}}$ and the MW halo DM contribution of $144\ \mathrm{pc\,cm^{-3}}$ expected from the Yamasaki & Totani (2020) halo model. The curved black solid line shows the best-fitting τ_s–DM relation of Galactic pulsars (Cordes, Ocker & Chatterjee 2022) with its 1σ range highlighted with black-dashed lines. We can see in Fig. 9 that FRB 20210405I's scattering time is larger than the scattering time expected from the Milky Way, which is also the lower DM limit for an extra-galactic source; however, it is consistent with the scattering-DM relation of Galactic pulsars. This implies that FRB 20210405Iś scattering time measurement is consistent with either an extra-galactic source or a source within the MW halo.

FRB 20210405I is located at a low-Galactic latitude of −4.597 deg, which means that its radio signal passed through the thick disc of the Milky Way. The best-fitting scattering index is

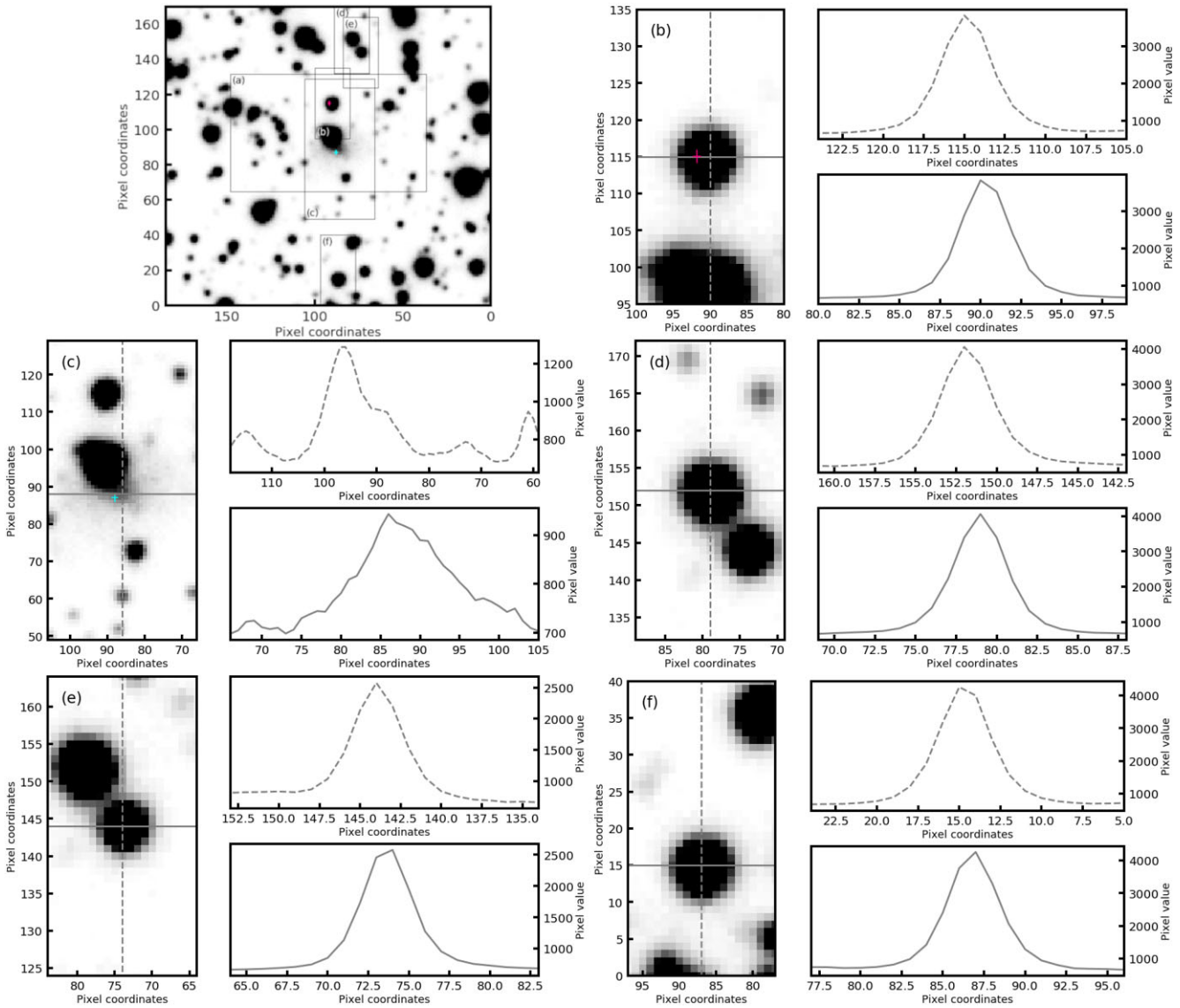

Figure 7. DECaPS VR stacked optical image showing the PSFs of the optical sources near FRB 20210405I. The top left panel shows the FoV around FRB 20210405I and the positions of the nearby sources. The region marked (a) is the region shown in Fig. 5. The other regions are shown in the other panels in this figure. Region/panel (b) includes the position of FRB 20210405I (marked with magenta cross-hairs) and shows the cross-section of the PSF of *Gaia* DR3 5938235492995353728. Region/panel (c) shows the position of the galaxy, with the position of the continuum radio source marked with cyan cross-hairs. We can see that the optical PSF of the galaxy is wide and irregular, while the PSF of *Gaia* DR3 5938235492995353728 and the nearby sources shown in panels (d)–(f) are approximately Gaussian, as expected for a point source.

-4.6 ± 0.1 (see subsection 3.3), which agrees well with the power-law index expected from Kolmogorov turbulence in ionized media, $-22/5 = -4.4$. It is also consistent with the spread in scattering indices $3 < \gamma_s < 4.5$ observed in Galactic radio pulsars (Oswald et al. 2021; Cordes, Ocker & Chatterjee 2022). The scattering time interpolated to 1 GHz is 9.7 ± 0.2 ms. The pulse broadening expected from the Milky Way ISM in that direction is 0.122 ms according to the NE2001 Galactic free-electron model (Cordes & Lazio 2002). The isotropic thin-screen scattering model describes the data well with profile residuals that appear normally distributed for both the band-integrated and sub-banded data. The profile data offer little room for deviations from the isotropic scattering regime.

5.1.4 *Luminosity*

We investigated the expected specific radio luminosity of FRB 20210405I to verify whether the expected energetics are consistent with the general population of FRBs. To do so, we computed the specific luminosity by multiplying the peak flux density of the burst with the square of the distance to the source. We consider two cases (1) FRB 20210405I lies within our Galaxy and (2) FRB 20210405I lies in the galaxy at a redshift of 0.066. In order to estimate the distance of FRB 20210405I in the galaxy, we used a DM range of 416 to 616 pc cm^{-3} and use the NE2001 electron density model to map the DM to a distance in the galaxy. Then we computed the specific luminosity for FRB 20210405I for this range of distances. The values for both cases were plotted on the specific luminosity

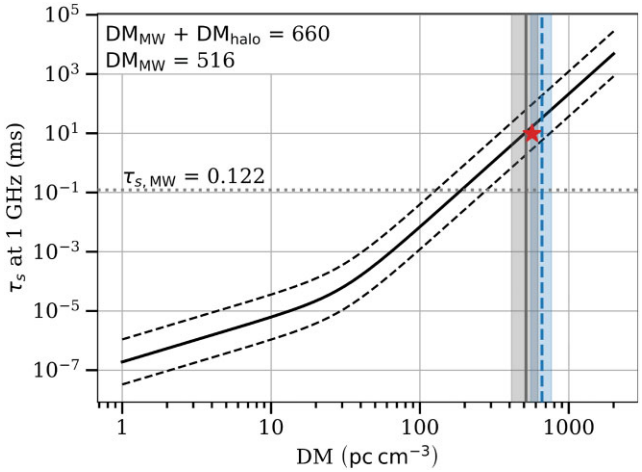

Figure 8. Location of FRB 20210405I (red star) in a scattering time, τ_s, versus DM diagram. $\tau_{s,MW}$ is the expected Milky Way scattering contribution. We highlight the τ_s – DM relation of Galactic pulsars and its 1σ uncertainty range with black lines. We also show the DM contributions and their uncertainty ranges from the ISM and the MW halo for that sightline, assuming the NE2001 free-electron model and the Yamasaki & Totani (2020) halo model.

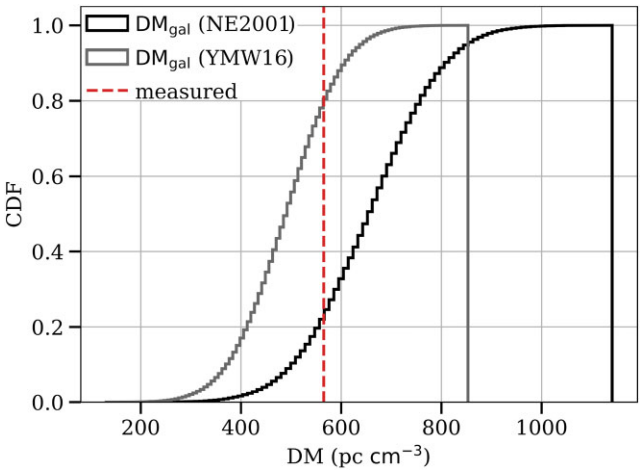

Figure 9. Cumulative density function of the total Galactic DM contribution DM$_{gal}$ = DM$_{ism}$ + DM$_{halo}$ for the NE2001 and YMW16 model and using the Yamasaki & Totani (2020) halo model. We assumed a 20 per cent uncertainty on the maximum integrated ISM contributions and a 40 per cent uncertainty on the MW halo component. The red vertical line marks FRB 20210405I's measured DM. The probabilities of FRB 20210405I being extra-galactic are ∼24 and ∼80 per cent, respectively.

versus burst width parameter space that shows different classes of coherently emitting transients (see Fig. 10). One can clearly see from the figure that if FRB 20210405I is associated with the optical galaxy at a redshift of 0.066 then the luminosity is consistent with the population of FRBs. Alternatively, if FRB 20210405I lies in our Galaxy, the burst has a higher specific luminosity than bursts from the magnetar XTE J1810−197 and stands out from the populations of RRATs, magnetars, pulsars based on luminosity and stands out from pulsar giant pulses based on time-scale.

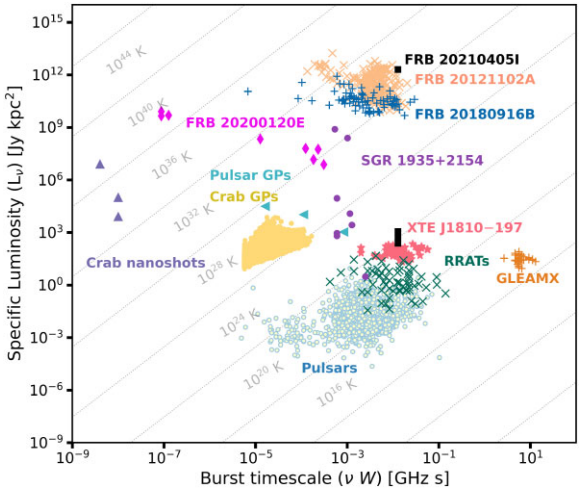

Figure 10. Specific luminosity versus burst duration plot for various coherently emitting radio transients (Cordes & McLaughlin 2003; Nimmo et al. 2022a). Grey lines indicate lines of constant brightness temperature. FRB 20210405I is marked in black twice in the plot, once assuming it is extra-galactic and once assuming it is Galactic.

5.1.5 *Association with 2MASS J1701249−4932475*

In order to robustly claim association of FRB 20210405I with the 2MASS J1701249−4932475, we computed the chance coincidence probability of spatial coincidence. For this we considered two cases separately (1) FRB 20210405I is Galactic and lies on top of 2MASS J1701249−4932475 in the sky plane and (2) FRB 20210405I is extra-galactic but originates in a different unseen host galaxy. For case 1, the probability of chance coincidence,

$$P(cc|l,b) = P(\text{2MASS J1701249} - 4932475, l, b), \quad (11)$$

where, P(2MASS J1701249-4932475, l, b) is the probability for a galaxy to be at a Galactic longitude l and latitude b. To obtain P(2MASS J1701249-4932475, l, b) out to the redshift of 2MASS J1701249−4932475, we used the same methodology as used by Campisi & Li (2008) and found a probability of 0.0025. Hence, for case 1, $P_{cc} \simeq 2.5 \times 10^{-3}$.

For case 2, we used the chance association probability methodology from Eftekhari & Berger (2017) and Aggarwal et al. (2021). For this case, we used the 99 per cent confidence upper limit of an unseen host redshift of 0.35. Using this, we obtained $P_{cc} \simeq$0.009. So for both cases, the value of P_{cc} is very low. Therefore, we conclude that FRB 20210405I is associated with 2MASS J1701249−4932475.

The angular offset between FRB 20210405I and the centre of the galaxy of 7.″4 at a luminosity distance of 296.8 Mpc corresponds to a projected physical offset of 10.65 kpc in the host galaxy reference frame. This places the FRB in the spiral arms or halo of the galaxy. This is at the high end of the offset distribution of well-localized FRBs and clearly above the median of 3.3 kpc (Heintz et al. 2020) but is consistent with two of the bursts, FRB 20190611B ($z = 0.3778$) and FRB 20191001A ($z = 0.2340$).

5.1.6 *Summary*

Neither the DM nor scattering properties of FRB 20210405I strongly support either a Galactic origin or an association with 2MASS J1701249−4932475 at $z = 0.066$. However, the specific luminosity favours the latter. We also show that the probability that the spatial coincidence between FRB 20210405I and 2MASS

J1701249−4932475 is chance coincidence is low. Therefore, we find it much more likely that FRB 20210405I is an FRB associated with 2MASS J1701249−4932475 as the DM, scattering, specific luminosity, and localization are all consistent with this conclusion. It is still possible for the FRB to originate within the Milky Way; however, this would require an unusually bright magnetar/pulsar burst and an improbable spatial coincidence.

The uncertainty in the Galactic or extra-galactic origin of this FRB highlights the uncertainty in our understanding of the Milky Way DM and particularly the Milky Way halo DM. This was also highlighted by Ravi et al. (2023) for FRB 20220319D. It is important to continue to test and expand our measurements of these as demonstrated by Cook et al. (2023). We are currently limited in our understanding and models in the Galactic Plane for both the Galactic and halo DM contributions. More FRB detections at lower Galactic latitudes will help to test and improve the models.

5.2 Comparison to previously identified FRB host galaxies

These results indicate that 2MASS J1701249−4932475 is an evolved massive galaxy with high metallicity as is typical at such high-stellar masses, but with very low star-formation. This possibly points towards even higher dust extinction in the host galaxy or to an early type spiral galaxy. The stellar mass and SFR are respectively at the higher and lower end of the FRB host population (Bhandari et al. 2022), extending it to massive, early type galaxies. A comparison of these characteristics with the hosts of other classes of transients, shows that these properties are completely different from those of the hosts of explosive transients such as long gamma-ray bursts (Vergani et al. 2017; Palmerio et al. 2019) and superluminous supernovae (Lunnan et al. 2014; Japelj et al. 2016). However, they can correspond to a subgroup of the host galaxy population of other kinds of core-collapse SN (such as Type II SN (Kelly et al. 2014; Lunnan et al. 2014)), if the real SFR is much higher than the reported lower limit. Some hosts of merger-driven transients such as short gamma-ray bursts (Berger 2014) have similar characteristics (see also Bhandari et al. 2022).

5.3 Searching for FRB 20210405I in past images

While FRB 20210405I was detected by MeerTRAP and ThunderKAT on 2021 April 05, ThunderKAT has been observing GX 339−4 weekly since September 2018 and will continued to do so until August 2023. MeerTRAP started observing commensally with ThunderKAT in September 2021. This means that there are ∼2 yr of weekly images prior to MeerTRAP observing with ThunderKAT where FRB 20210405I may be detected if it is repeating and bright enough to be detected in 8 s images. Producing thousands of 8 s images is time consuming, and not all of the available weekly epochs have been imaged in 8 s slices. The list of epochs and the number of 8 s images available for each epoch is shown in Table A1 in Appendix A. We have searched 100 epochs with a total of 8049 × 8 s images observed prior to September 2021 for a repeat burst from FRB 20210405I, using a match radius of 3′. We use a radius of 3′ as the astrometric offset of each image can be different prior to correction. We present some possible detections with low-S/N in Table 3.

At the time of writing there were ∼100 weekly 10 min ThunderKAT observations since MeerTRAP started observing commensally with ThunderKAT in September 2021. This means that there has been approximately 17 h of MeerTRAP monitoring of the field. We have not detected any further bursts from FRB 20210405I with MeerTRAP. We found two low-S/N image-plane transient candidates in 8 s images of the field prior to September 2021. Due to the low-S/N of these sources and the 8 s time resolution, we cannot confirm whether these are artefacts or repeat bursts from the FRB source. MeerTRAP will continue to observe commensally with ThunderKAT during their weekly observations of GX 339−4.

Table 3. Low S/N detections of sources in 8 s images that are within 3′ of FRB 20210405I, the first row shows the detection of FRB 20210405I on 2021 April 05. The positions quoted here have been astrometrically corrected and the separation is the angular separation between the source and the FRB 20210405I position. S_ν is the MFS (1283 MHz) peak flux density that has not had a primary beam correction applied.

Date	Coordinates (J2000)	Sep (′)	S/N	S_ν (mJy)
2021 Apr 05	$17^h01^m21\overset{s}{.}5 \pm 0\overset{\prime\prime}{.}4$ $-49°32'42\overset{\prime\prime}{.}5 \pm 0\overset{\prime\prime}{.}5$	0	25	5.2 ± 0.2
2019 Aug 04	$17^h01^m21\overset{s}{.}5 \pm 0\overset{\prime\prime}{.}8$ $-49°32'41\overset{\prime\prime}{.}5 \pm 2\overset{\prime\prime}{.}0$	1.0	4	0.9 ± 0.2
2020 Apr 18	$17^h01^m21\overset{s}{.}7 \pm 0\overset{\prime\prime}{.}9$ $-49°32'43\overset{\prime\prime}{.}2 \pm 2\overset{\prime\prime}{.}0$	1.9	4	0.7 ± 0.2

5.4 Future FRB localization prospects

FRB 20210405I is the first sub-arcsecond localized FRB using the MeerKAT telescope, and this localization was made possible by the commensal nature of the MeerTRAP project. As MeerTRAP observes commensally with all MeerKAT LSPs, we can use the 8 s images from the LSP observations to localize bright FRBs. This demonstrates the power of commensal searches for single pulses. However, only FRBs with high-S/N can be localized in second-long images. We are currently working to implement a fast imaging pipeline as part of MeerTRAP. When MeerTRAP is triggered by a single pulse we can save the transient buffer data as phase delay corrected voltages. These data are typically <1 s long, and we slice around the DM of the burst. We can then image these data offline to rapidly produce images and localize the burst. This pipeline will be an important tool for localizing MeerTRAP FRBs and expanding the sample of FRBs associated with host galaxies.

6 CONCLUSIONS

We detected a new FRB, using MeerKAT and the MeerTRAP backend. At the time of FRB 20210405I's detection, MeerTRAP was observing commensally with ThunderKAT, which enabled us to use the ThunderKAT 8 s images to localize the FRB with sub-arcsecond precision. We used the specific luminosity and chance coincidence probability to determine that FRB 20210405I is most likely of extra-galactic origin and is associated with nearby galaxy 2MASS J1701249−4932475. We determined that the host galaxy is a disc/spiral galaxy at a redshift of $z = 0.066$. However, there is a discrepancy between the YMW16 and NE2001 predictions for the Milky Way DM which means that there could be some uncertainty about its true location based on the measure DM alone. However the combination of the association with the nearby host galaxy, the predicted luminosity based on it being located in the proposed host, and the scattering properties support it as being extra-galactic. This FRB highlights the uncertainty in the Milky Way DM and halo models that should be further explored with a larger sample of localized FRBs. FRB 20210405I is the first FRB localized to sub-arcsecond precision using MeerKAT.

ACKNOWLEDGEMENTS

We thank Chris Williams for all his assistance in getting the MeerTRAP pipeline up and running and Jim Cordes for helpful discussions. We would like to thank the operators, SARAO staff and ThunderKAT LSP team. LND, MC, FJ, KMR, BWS, MCB, MM, VM, SS, and MPS acknowledge support from the European Research Council (ERC) under the European Union's Horizon 2020 research and innovation programme (grant agreement no. 694745). MC acknowledges support of an Australian Research Council Discovery Early Career Research Award (project number DE220100819) funded by the Australian Government and the Australian Research Council Centre of Excellence for All Sky Astrophysics in 3 Dimensions (ASTRO 3D), through project number CE170100013. RKK and HC acknowledge the support the South African Department of Science and Innovation and the National Research Foundation received through the SARAO SARCHI Research Chair. HC is supported by Key Research Project of Zhejiang Lab (No. 2021PE0AC03). DAHB acknowledges support from the South African National Research Foundation. PAW acknowledges financial support from the NRF (grant no. 129359) and UCT. MG is supported by the EU Horizon 2020 research and innovation programme under grant agreement number 101004719. The MeerKAT telescope is operated by the South African Radio Astronomy Observatory (SARAO), which is a facility of the National Research Foundation, an agency of the Department of Science and Innovation. We acknowledge use of the Inter-University Institute for Data Intensive Astronomy (IDIA) data intensive research cloud for data processing. IDIA is a South African university partnership involving the University of Cape Town, the University of Pretoria and the University of the Western Cape. The authors also acknowledge the usage of TRAPUM infrastructure funded and installed by the Max-Planck-Institut für Radioastronomie and the Max-Planck-Gesellschaft. The SALT observations were obtained under the SALT Large Science Programme on transients (2018-2-LSP-001; PI: DAHB). Polish participation in SALT is funded by grant number MEiN nr 2021/WK/01. This work has made use of data from the European Space Agency (ESA) mission *Gaia*.[14] Funding for the DPAC has been provided by national institutions, in particular the institutions participating in the *Gaia* Multilateral Agreement. This research made use of Astropy,[15] a community-developed core PYTHON package for Astronomy (Astropy Collaboration et al. 2013, 2018). This research made use of APLPY, an open-source plotting package for PYTHON (Robitaille & Bressert 2012). This research uses services or data provided by the Astro Data Lab at NSF's National Optical-Infrared Astronomy Research Laboratory. NOIRLab is operated by the Association of Universities for Research in Astronomy (AURA), Inc. under a cooperative agreement with the National Science Foundation. This research has made use of the VizieR catalogue access tool, CDS, Strasbourg, France.[16] The original description of the VizieR service was published in Ochsenbein, Bauer & Marcout (2000). This research has made use of the SIMBAD data base, operated at CDS, Strasbourg, France (Wenger et al. 2000). This research has made use of NASA's Astrophysics Data System Bibliographic Services.[17] LND would like to acknowledge the traditional owners of the land where most of her work was performed: the Wurundjeri People of the Woi worrung Nation, the Whadjuk people of the Noongar Nation and the Gadigal People of the Eora Nation. We would like to thank the referee for their constructive comments and help in improving this manuscript.

[14] https://www.cosmos.esa.int/⟨0:italic⟩Gaia⟨/0:italic⟩, processed by the *Gaia* Data Processing and Analysis Consortium (DPAC, https://www.cosmos.esa.int/web/⟨0:italic⟩Gaia⟨/0:italic⟩/dpac/consortium)

[15] http://www.astropy.org

[16] 10.26093/cds/vizier

[17] https://ui.adsabs.harvard.edu/

7 DATA AVAILABILITY

AstroAccelerate is available here: https://github.com/AstroAccelerateOrg/astro-accelerate. The `LOFAR Transients Pipeline` is available here: https://tkp.readthedocs.io/en/latest/index.html. The code for performing the astrometry is available on Zenodo: https://doi.org/10.5281/zenodo.4921715.

REFERENCES

Adámek K., Armour W., 2020, ApJS, 247, 56
Aggarwal K., Budavári T., Deller A. T., Eftekhari T., James C. W., Prochaska J. X., Tendulkar S. P., 2021, ApJ, 911, L95
Andersson A., et al., 2022, MNRAS, 513, 3482
Armour W., et al., 2012, in Ballester P., Egret D., Lorente N. P. F., eds, ASP Conf. Ser. Vol. 461, Astronomical Data Analysis Software and Systems XXI. p. 33 preprint (arXiv:1111.6399)
Astropy Collaboration et al., 2013, A&A, 558, 33
Astropy Collaboration et al., 2018, AJ, 156, 123
Bannister K. W., et al., 2019, Science, 365, 565
Berger E., 2014, ARA&A, 52, 43
Bezuidenhout M. C., et al., 2022, MNRAS, 512, 1483
Bhandari S., et al., 2020, ApJ, 901, L20
Bhandari S., et al., 2022, AJ, 163, 69
Bhandari S., et al., 2023, ApJ, 948, L67
Bhardwaj M., et al., 2021, ApJ, 910, L18
Briggs D. S., 1995, in American Astronomical Society Meeting Abstracts. p. 112.02
Bright J. S., et al., 2020, Nature Astron., 4, 697
Buckley D. A. H., Swart G. P., Meiring J. G., 2006, in Stepp L. M., ed., Proc. SPIE Vol. 6267, Society of Photo-Optical Instrumentation Engineers (SPIE) Conference Series. SPIE, Bellingham, p. 62670Z
Burgh E. B., Nordsieck K. H., Kobulnicky H. A., Williams T. B., O'Donoghue D., Smith M. P., Percival J. W., 2003, in Iye M., Moorwood A. F. M., eds, Proc. SPIE, Vol. 4841, Instrument Design and Performance for Optical/Infrared Ground-based Telescopes. SPIE, Bellingham, p. 1463
Caleb M., Keane E., 2021, Universe, 7, 453
Caleb M., et al., 2020, MNRAS, 496, 4565
Camilo F., et al., 2018, ApJ, 856, L180
Campisi M. A., Li L.-X., 2008, MNRAS, 391, 935
Charlot P., et al., 2020, A&A, 644, 159
Chatterjee S., 2021, Astronomy and Geophysics, 62, 1
Chatterjee S., et al., 2017, Nature, 541, 58
Cook A. M., et al., 2023, ApJ, 946, L58
Cordes J. M., Chatterjee S., 2019, ARA&A, 57, 417
Cordes J. M., Lazio T. J. W., 2001, ApJ, 549, L997
Cordes J. M., Lazio T. J. W., 2002, preprint(astro-ph/0207156)
Cordes J. M., McLaughlin M. A., 2003, ApJ, 596, L1142
Cordes J. M., Ocker S. K., Chatterjee S., 2022, ApJ, 931, L88
Crawford S. M. et al., 2010, in Silva D. R., Peck A. B., Soifer T. B., eds, Proc. SPIE, Vol. 7737, Observatory Operations: Strategies, Processes, and Systems III. SPIE, Bellingham, p. 773725
Dewey R. J., Taylor J. H., Weisberg J. M., Stokes G. H., 1985, ApJ, 294, L25
Driessen L. N., et al., 2020, MNRAS, 491, 560
Driessen L. N., et al., 2022a, MNRAS 512 5037
Driessen L. N., Williams D. R. A., McDonald I., Stappers B. W., Buckley D. A. H., Fender R. P., Woudt P. A., 2022b, MNRAS, 510, 1083
Eftekhari T., Berger E., 2017, ApJ, 849, L162
Fender R., et al., 2016, in Taylor R., Camilo F., Leeuw L., Moodley K., eds, MeerKAT Science: On the Pathway to the SKA. p. 13 preprint (arXiv:1711.04132)

Foreman-Mackey D., Hogg D. W., Lang D., Goodman J., 2013, PASP, 125, 306
Gaia Collaboration et al., 2016, A&A, 595, 1
Gaia Collaboration et al., 2022, A&A, 667, 148
Gaia Collaboration et al., 2023, A&A, 674, 1
Gordon A. C., et al., 2023, ApJ, 954, L80
Heintz K. E., et al., 2020, ApJ, 903, L152
Hewitt D. M., et al., 2020, MNRAS, 496, 2542
Hotan A. W., et al., 2021, PASA, 38, e009
James C. W., Prochaska J. X., Macquart J. P., North-Hickey F. O., Bannister K. W., Dunning A., 2022a, MNRAS, 509, 4775
James C. W., et al., 2022b, MNRAS, 516, 4862
Jankowski F., 2022, Scatfit: Scattering fits of time domain radio signals (Fast Radio Bursts or pulsars), Astrophysics Source Code Library, record ascl:2208.003
Jankowski F., et al., 2019, MNRAS, 484, 3691
Jankowski F., et al., 2022, in Ruiz J. E., Pierfedereci F., Teuben P., eds, ASP Conf. Ser. Vol. 532, Astronomical Society of the Pacific Conference Series. p. 273 preprint (arXiv:2012.05173)
Jankowski F., et al., 2023, MNRAS, 524, 4275
Japelj J., Vergani S. D., Salvaterra R., Hunt L. K., Mannucci F., 2016, A&A, 593, 115
Kelly P. L., Filippenko A. V., Modjaz M., Kocevski D., 2014, ApJ, 789, L23
Kirsten F., et al., 2022, Nature, 602, 585
Law C. J., et al., 2020, ApJ, 899, L161
Lunnan R., et al., 2014, ApJ, 787, L138
Luo R., et al., 2020, Nature, 586, 693
Ma C., et al., 1998, AJ, 116, 516
Macquart J. P., et al., 2020, Nature, 581, 391
Maiolino R., et al., 2008, A&A, 488, 463
Marcote B., et al., 2017, ApJ, 834, L8
Marcote B., et al., 2020, Nature, 577, 190
Marcote B., et al., 2021, ATel, 14603, 1
McConnell D., Sadler E. M., Murphy T., Ekers R. D., 2012, MNRAS, 422, 1527
McMullin J. P., Waters B., Schiebel D., Young W., Golap K., 2007, in Shaw R. A., Hill F., Bell D. J., eds, ASP Conf. Ser. Vol. 376, Astronomical Data Analysis Software and Systems XVI. Astron. Soc. Pac., San Francisco, p. 127
Meyer M., Robotham A., Obreschkow D., Westmeier T., Duffy A. R., Staveley-Smith L., 2017, PASA, 34, 52
Michilli D., et al., 2018, Nature, 553, 182
Newville M., Stensitzki T., Allen D. B., Rawlik M., Ingargiola A., Nelson A., 2016, Lmfit: Non-Linear Least-Square Minimization and Curve-Fitting for Python, record ascl:1606.014
Nimmo K., et al., 2022a, Nature Astron., 6, 393
Nimmo K., et al., 2022b, ApJ, 927, L3
Niu C. H., et al., 2022, Nature, 606, 873
Ochsenbein F., Bauer P., Marcout J., 2000, A&AS, 143, 23
Offringa A. R., 2010, AOFlagger: RFI Software, record ascl:1010.017
Offringa A. R., van de Gronde J. J., Roerdink J. B. T. M., 2012, A&A, 539
Offringa A. R., et al., 2014, MNRAS, 444, 606
Oswald L. S., et al., 2021, MNRAS, 504, 1115
Palmerio J. T., et al., 2019, A&A, 623, 26
Pei Y. C., 1992, ApJ, 395, L130
Perley R. A., Chandler C. J., Butler B. J., Wrobel J. M., 2011, ApJ, 739, L1
Petroff E., Hessels J. W. T., Lorimer D. R., 2019, A&A Rev., 27, 4
Petroff E., Hessels J. W. T., Lorimer D. R., 2022, A&A Rev., 30, 2
Petrov L., Phillips C., Bertarini A., Murphy T., Sadler E. M., 2011, MNRAS, 414, 2528
Prochaska J. X., et al., 2019, Science, 366, 231
Rajwade K. M., et al., 2022, MNRAS, 514, 1961
Ravi V., 2023, ATel, 16191, 1
Ravi V., et al., 2019, Nature, 572, 352
Ravi V., et al., 2023, preprint (arXiv:2301.01000)
Rhodes L., et al., 2020, MNRAS, 496, 3326
Riad I. F., Kraan-Korteweg R. C., Woudt P. A., 2010, MNRAS, 401, 924
Robitaille T., Bressert E., 2012, APLpy: Astronomical Plotting Library in Python, Astrophysics Source Code Library, record ascl:1208.017
Rowlinson A., et al., 2022, MNRAS, 517, 2894
Russell T. D., et al., 2019, ApJ, 883, L198
Ryder S. D., et al., 2023, Science, 382, 294
Salpeter E. E., 1955, ApJ, 121, L161
Sanidas S., Caleb M., Driessen L., Morello V., Rajwade K., Stappers B. W., Cambridge University Press Cambridge, United Kingdom, 2018, in Weltevrede P., Perera B. B. P., Preston L. L., Sanidas S., eds, Pulsar Astrophysics the Next Fifty Years, Vol. 337. p. 406
Schlafly E. F., Finkbeiner D. P., 2011, ApJ, 737, L103
Schlafly E. F., et al., 2018, ApJS, 234, 39
Skrutskie M. F., et al., 2006, AJ, 131, 1163
Swinbank J. D., et al., 2015, Astron. Comput., 11, 25
Tasse C., et al., 2018, A&A, 611
Tendulkar S. P., et al., 2017, ApJ, 834, L7
Tiburzi C., et al., 2021, A&A, 647, 84
Tremou E., et al., 2020, MNRAS, 493, 132
van den Eijnden J., Fender R., Miller-Jones J. C. A., Russell T. D., Saikia P., Sivakoff G. R., Carotenuto F., 2022, MNRAS, 516, 2641
Vergani S. D., et al., 2017, A&A, 599, 120
Wang N., Manchester R. N., Johnston S., 2007, MNRAS, 377, 1383
Wenger M., et al., 2000, A&AS, 143, 9
Williams D. R. A., et al., 2020, MNRAS, 491, 29
Wright E. L., et al., 2010, AJ, 140, 1868
Yamasaki S., Totani T., 2020, ApJ, 888, L105
Yao J. M., Manchester R. N., Wang N., 2017, ApJ, 835, L29
Zhang B., 2018, ApJ, 854, L21

APPENDIX A: REPEAT OBSERVATIONS OF THE GX 339−4 FIELD

Table A1. Date of each ThunderKAT observation of GX 339−4 where we have imaged the epoch in 8 s intervals. The number of 8 s intervals that have been imaged per epoch is shown here.

Date	Number of images	Date	Number of images	Date	Number of images
2018 Sep 28	27	2019 May 25	75	2020 Jan 03	75
2018 Oct 05	109	2019 May 31	74	2020 Jan 10	73
2018 Oct 11	112	2019 June 08	73	2020 Jan 20	75
2018 Oct 12	112	2019 June 16	74	2020 Jan 25	74
2018 Oct 19	109	2019 June 24	74	2020 Feb 02	73
2018 Oct 27	111	2019 June 30	75	2020 Feb 08	74
2018 Nov 03	112	2019 July 07	74	2020 Feb 15	75
2018 Nov 10	110	2019 July 14	73	2020 Feb 21	74
2018 Nov 17	112	2019 July 22	75	2020 Mar 02	73
2018 Nov 24	112	2019 July 27	74	2020 Mar 09	74
2018 Dec 08	111	2019 Aug 04	74	2020 Mar 14	75
2018 Dec 15	112	2019 Aug 10	75	2020 Mar 21	74
2018 Dec 22	112	2019 Aug 16	74	2020 Mar 29	74
2018 Dec 29	111	2019 Aug 23	56	2020 Apr 03	31
2019 Jan 05	112	2019 Aug 31	75	2020 Apr 10	75
2019 Jan 12	112	2019 Sep 07	74	2020 Apr 18	73
2019 Jan 19	112	2019 Sep 14	74	2020 Apr 25	74
2019 Jan 26	112	2019 Sep 21	74	2020 May 01	74
2019 Feb 01	111	2019 Sep 29	74	2020 May 09	74
2019 Feb 09	111	2019 Oct 06	74	2020 May 17	74
2019 Feb 16	111	2019 Oct 12	74	2020 June 08	75
2019 Feb 23	111	2019 Oct 19	74	2020 June 14	74
2019 Mar 01	11	2019 Oct 26	74	2020 June 17	73
2019 Mar 09	111	2019 Nov 01	73	2020 June 19	74
2019 Mar 18	72	2019 Nov 10	74	2020 June 26	74
2019 Mar 25	74	2019 Nov 17	74	2020 July 04	74
2019 Apr 01	59	2019 Nov 24	74	2020 July 12	75
2019 Apr 09	64	2019 Nov 30	74	2020 July 19	74
2019 Apr 15	75	2019 Dec 02	111	2020 July 26	75
2019 Apr 20	74	2019 Dec 07	74	2020 Aug 01	74
2019 Apr 29	73	2019 Dec 15	74	2020 Aug 08	74
2019 May 05	60	2019 Dec 20	74	2020 Aug 15	74
2019 May 11	72	2019 Dec 28	74	2020 Aug 22	75
2019 May 18	74				

This paper has been typeset from a TEX/LATEX file prepared by the author.